Mechanical characterization of hydrogen embrittlement in a gaseous environment: An innovative test setup using sub-size specimens

Yazid Madi, L.M. Santana, S. Belkacemi, V. Farrugia, A. Meddour, P-J. Marchais, M. Bertin, J. Furtado

Engineering Failure Analysis 162 (2024) 108362

Contents lists available at ScienceDirect

Engineering Failure Analysis

journal homepage: www.elsevier.com/locate/engfailanal

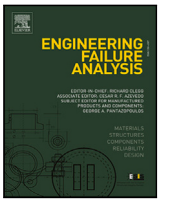

Mechanical characterization of hydrogen embrittlement in a gaseous environment: An innovative test setup using sub-size specimens

Y. Madi [a,*], L.M. Santana [a,c,d], S. Belkacemi [a,b], V. Farrugia [a,b], A. Meddour [a], P-J. Marchais [d], M. Bertin [b], J. Furtado [c]

[a] Centre des Matériaux, MINES Paris, Université PSL, CNRS UMR 7633, France
[b] RICE GRTgaz, France
[c] Air Liquide, Innovation Campus Paris, France
[d] Mannessmann Precision Tubes France SAS, France

ARTICLE INFO

Keywords:
Gaseous Hydrogen embrittlement
Mini-specimen
Steel
Tensile
Toughness

ABSTRACT

Hydrogen embrittlement (HE) of steels in the presence of gaseous hydrogen poses a challenge to the safe transportation of hydrogen through pipelines. The use of sub-size specimens machined from coupons extracted from pipes is proposed for monitoring the degradation of material properties over the entire operational life. The objective of this paper is to present a methodology based on the sub-size specimens using a machine developed to operate with a small volume of gaseous hydrogen, up to a pressure of 250 bars, and test control using Edge Tracing (ET) technique. Tensile and toughness mini-specimens extracted from a E355 mod. steel grade are employed for this study. Reliable results are obtained using tensile mini-specimens with 1.2 and 2.4 mm diameters, tested under both air and gaseous H_2. Toughness tests are conducted using mini-specimens with a thickness of 5 mm. These tests monitored the Load Line Opening Displacement (LLOD) and the Opening Angle are monitored during the tests through ET technique, allowing for the determination of $J - \Delta a$ and $\delta - \Delta a$ plots under both air and gaseous H_2 conditions. The results uncover the impact of H_2 pressure and specimen dimensions on hydrogen embrittlement, leading to the computation of Hydrogen Embrittlement Indexes through various methods. The insights gained from this study establish the necessary foundations for the utilization of mini-specimens in characterizing hydrogen embrittlement.

1. Introduction

Europe is firmly committed to a sustainable energy transition, with ambitious carbon neutrality goals by 2050. France has set a target to reduce greenhouse gas emissions by 33% by 2030 compared to 2022. In this context, the development of renewable and low-carbon hydrogen becomes a strategic priority. As an energy vector, renewable hydrogen offers the advantage of not emitting greenhouse gases during its use and production. It also presents significant potential as a means of electricity storage, thus contributing to the balance of the electrical system.

Furthermore, the European Hydrogen Backbone (EHB) initiative plays a key role in the decarbonization of Europe, highlighting the crucial importance of the hydrogen infrastructure, [1,2]. This initiative envisages the combined use of repurposed existing natural

* Corresponding author.
E-mail address: yazid.madi@minesparis.psl.eu (Y. Madi).

https://doi.org/10.1016/j.engfailanal.2024.108362
Received 22 January 2024; Received in revised form 6 April 2024; Accepted 22 April 2024
Available online 3 May 2024

gas pipelines and new pipelines to create a competitive, renewable, and low-carbon pan-European hydrogen market. By 2040, the network is expected to consist of approximately 60% repurposed natural gas pipelines and 40% new pipelines. The repurposing of existing pipelines, potentially more cost-effective – estimated at just 10% of the cost of constructing new ones – will, however, be subject to a multitude of considerations. These factors include availability, implementation timelines, long-term sustainability, ecological impact, land footprint, and societal value, all of which are critical in the decision-making process for repurposing.

Hydrogen embrittlement (HE) of steels in the presence of hydrogen gas presents a significant challenge to the safe transportation of hydrogen via pipelines. This aspect has been the subject of several recent literature reviews, [3–6], providing a detailed exploration of relevant considerations in addressing HE in pipeline transportation. This phenomenon leads to a reduction in both ductility and fracture toughness of the steel, posing a major obstacle to the utilization of existing pipeline systems for pressurized gaseous hydrogen transport. Before these systems can be deemed fit for this new purpose, a thorough evaluation of their serviceability is imperative, [7,8]. The severity of hydrogen embrittlement is influenced by a combination of mechanical, material, and environmental factors. Research suggests that the introduction of gas impurities, acting as inhibitors, into the hydrogen gas mixture can mitigate the uptake of hydrogen by pipeline steel.

Several methods exist for investigating HE in metallic materials, with most research employing electrochemical hydrogen charging due to its ease of implementation. However, this approach is not entirely accurate for materials exposed to gaseous hydrogen in pipeline transportation, as it necessitates coupling hydrogen charging with mechanical loading. Additionally, due to the high hydrogen diffusion, testing typically requires specialized and expensive equipment designed for pressurized environments, which also entails stringent safety measures due to the explosive risks involved. On the other hand, load and strain measurements are often conducted using electrical resistance strain gauges, which are prone to drift in high-pressure hydrogen gas environment, [9,10]. An alternative method, [11–13], involves using tubular tensile specimens filled with pressurized gaseous hydrogen to study hydrogen embrittlement. While this method provides a direct approach to investigating HE under conditions akin to pipeline transportation, it is limited to tensile specimens without pre-existing cracks.

To simplify and monitor the evolution in material properties during the lifetime of hydrogen transport systems, the use of subsize-specimens, machined from extracted coupons, is proposed, [14,15]. In the literature, the use of mini flat tensile specimens is widely accepted for characterization of anisotropy, size effect and monitoring of in-service degradation [16–19]. Nevertheless, it remains imperative to rigorously assess numerous factors that can influence the quality and accuracy of results, especially for smooth tensile specimen geometries, including: machining and surface preparation; metrology; ratio of microstructural grain size to specimen size; tensile test setup and resolution of load cells and transducers. However, the experimental evaluation of toughness using subsize-specimens is less developed. The use of mini-toughness specimens has been developed in the nuclear industry for studying the ductile-to-brittle transition in irradiated steels of pressure vessels. These are primarily Compact Tension (CT) type specimens, which are machined from the undeformed parts of broken standard Charpy specimens. This technique is employed by [20–22] and comparisons with standard-sized specimens demonstrate that they are well-suited for measuring mechanical fracture properties, as long as scale effects are properly considered. Particularly, thin-walled tubes in gas transport, which cannot accommodate standard-sized specimen extraction, represent a similar challenge. To be considered valid, toughness tests must be performed on sufficiently large specimens. According to the ASTM E1820 standard [23], the maximum J-integral capacity that a specimen can achieve is determined by the following:

$$J_{\max} \leq \frac{1}{10} \min(B, b_0)\sigma_Y \tag{1}$$

where, B represents the specimen's thickness, b_0 the initial ligament length, and σ_Y the average of yield stress and tensile strength. This criterion ensures that the plasticized zone is significantly smaller than the specimen thickness and ligament size, indicating that the process zone is also substantially smaller than these dimensions. However, due to hydrogen embrittlement impact on material properties, which results in reduced toughness and a smaller plasticized zone, meeting the standard's size requirements becomes more feasible. Even if the tests do not conform to standard validity, these specimens are still valuable for comparing different loading conditions within a specific material, or for comparing various materials extracted from different parts under a given condition.

In this study, a specialized gaseous pressurized hydrogen machine is designed to perform low strain rate tests for subsize specimens. The chamber's volume is minimized, substantially mitigating explosive risks. Additionally, an optical extensometer employing Edge Tracing (ET) technique, [24], outside the chamber is developed to measure local specimen strain and control machine displacement during mechanical tests. The aim of this paper is to present a methodology based on the sub-size specimens using the developed tensile machine. The application of this methodology is then demonstrated on a modern ferritic-pearlitic material, selected for its isotropic behavior and its excellent ductility and toughness properties. Its composition is closely related to that of pipeline materials used for natural gas transportation. This approach aims to establish the necessary foundations for exploring vintage materials with more complex behaviors (anisotropy, welds, gradients, etc.), which will be essential for the conversion of existing pipeline networks.

2. Gaseous hydrogen setup for sub-size specimens

In this section, the development and setup of a new testing machine designed for experiments with hydrogen are detailed. Methods for measuring local displacements based on ET method are described, followed by a discussion on machine control derived from these measurements. Importantly, the machine conducts rigorous analyses of gas impurities downstream, crucial for maintaining a reproducible and accurate testing environment.

2.1. Description of the setup

Fig. 1 describes the setup developed for this study. A specialized high-pressure chamber is introduced. The chamber is designed for testing in no-ATEX conditions and confined spaces, thus requiring smaller test specimens. Outfitted with four sapphire windows, it enables the utilization of the Edge Tracing (ET) technique for optical extensometry as described in [24]. This ensures accurate measurements without the need for internal mechanical devices, and it remains unaffected by time-dependent drift during exposure to hydrogen gas. Backlighting is a technique where the object to be measured is positioned between an LED light source and a camera. A notable adaptation is the integration of a Keyence XG-X2800 controller. Initially designed for industrial product measurement and quality control, this controller has been adapted to support the ET technique, allowing for real-time communication with the MTS machine controller.

Considering the impact of friction forces from dynamic seals on the load line, the chamber includes an internal load cell capacity of 5 kN for a direct measurement of the test specimen's mechanical load. One challenge associated with using this strain gauge-based load cell is the tendency of the output signal to drift during the initial stages of hydrogen gas exposure, [9,10]. To address this issue, the load cell output is stabilized prior to initiating any tests, and the calibration factor is consistently checked to ensure it remains unchanged, with validations carried out at regular intervals.

Addressing the question of environmental control within the hydrogen chamber, the setup integrates comprehensive measures for impurity analysis, focusing on humidity and oxygen levels. This approach is crucial for ensuring a safe and precise testing environment. The procedures include securing system tightness and minimizing contaminant levels in the testing gas. Prior to any experimental runs, inerting procedures are carried out, and the autoclave's tightness is meticulously verified. Various procedures were assessed at the beginning of the test campaign to establish a secure and optimal testing environment. The gas analysis system features two electrochemical analysis cells for oxygen detection: a cell for high oxygen content (percent cell) and a cell for measurements below 200 volume parts per million (vppm), with a resolution up to 0.4 vppm for measurements below 10 vppm (Accurate RACE). Moisture analysis is facilitated by a stainless steel drying head with reduced volume, ensuring rapid transitions from dry to humid environments and an accuracy of ±2 °C dew point, approximately ±1.6 vppm. The system is designed to introduce a controlled small leak flow (1 liter/min) for measurements, allowing for the acquisition of real-time data for both oxygen and moisture content.

A modified dynamic MTS servo-hydraulic Landmarks machine with a proper program configuration is used. Very low strain rate testing can be reached (0.3 μm/min, $\dot{\epsilon} = 10^{-6}$/s for sub-size smooth tensile specimens), accomplished through the combination of a low-flow servo valve, super clean oil and a precise displacement sensor (MTS 632.06 H-33, ±2 mm travel displacement gauge) to control the load line rather than using the machine's linear variable differential transformer (LVDT). This specific configuration is inspired by methodologies outlined in [25]. The importance of the various components of the closed-loop controlled system and the test configuration is reviewed in [26].

Additionally, the system facilitates real-time communication between the MTS and Keyence controllers via the EtherCAT protocol. This feature allows for instantaneous adjustments through the MTS TestSuite program, providing precise regulation of the displacement gauge during experiments. These features collectively contribute to a setup that is not only innovative but also highly responsive and precise in its operations.

2.2. Gas analysis and inertization methodology

The purity of hydrogen gas in test conditions is a critical factor that significantly influences the outcomes of experiments, [27]. Adhering to standards such as ANSI/CSA CHMC-1(2014), [28], it is essential to ensure that the source gas purity aligns with the specifications outlined in CGA G-5.3. This involves not only the selection of high-quality source gas but also meticulous purging processes to maintain purity levels. It is crucial to recognize that the purity of the test gas should not be presumed to be equivalent to that of the source gas. Instead, it must be explicitly verified through the analysis of gas testing chamber. Key purity criteria include limiting oxygen content to less than or equal to 2 volume parts per million (vppm) and moisture or water content to less than or equal to 10 vppm.

For our experiments, hydrogen gas of 6.0 quality (99.9999% purity, with oxygen levels capped at 0.5 vppm) was utilized. To secure the most favorable testing conditions, we evaluated various preparatory procedures before launching the test campaign. The initial inertization process comprised several stages: (a) three nitrogen purges; (b) vacuum application; (c) leak testing with helium; (d) a second vacuum; and (e) hydrogen fill. This sequence was repeated with intervals, measuring oxygen concentration post each step. Post step (a), oxygen levels hovered around 480 vppm. Surprisingly, after vacuum application and helium testing (steps b and c), oxygen levels rose to approximately 4250 vppm, and the process concluded with oxygen at 3700 vppm, indicating an ineffective inertization, due to probably the entrance of air in the system during the vacuum.

Considering this inefficiency, a refined procedure to control gas impurities is proposed. Fig. 2 illustrates the autoclave pressure progression during the enhanced inertization method, now standardized owing to its efficacy in achieving the desired inert state. The revised steps are: (a) triple nitrogen purges; (b) a ten-minute nitrogen sweep; (c) helium leak check; and (d) pressurizing with hydrogen beyond test requirements, followed by gas analysis to confirm low oxygen levels prior to testing. Subsequent analysis confirmed that omitting the vacuum step in favor of a nitrogen sweep before helium addition markedly reduced oxygen content to 13.5 vppm. Finally, hydrogen injection reduced the oxygen level to below the limit detection of the accurate cell, thereby validating the improved procedure. Furthermore, after the completion of each mechanical test, the oxygen level is always analyzed to reaffirm the purity of the test environment, ensuring that the results are not compromised by environmental variables.

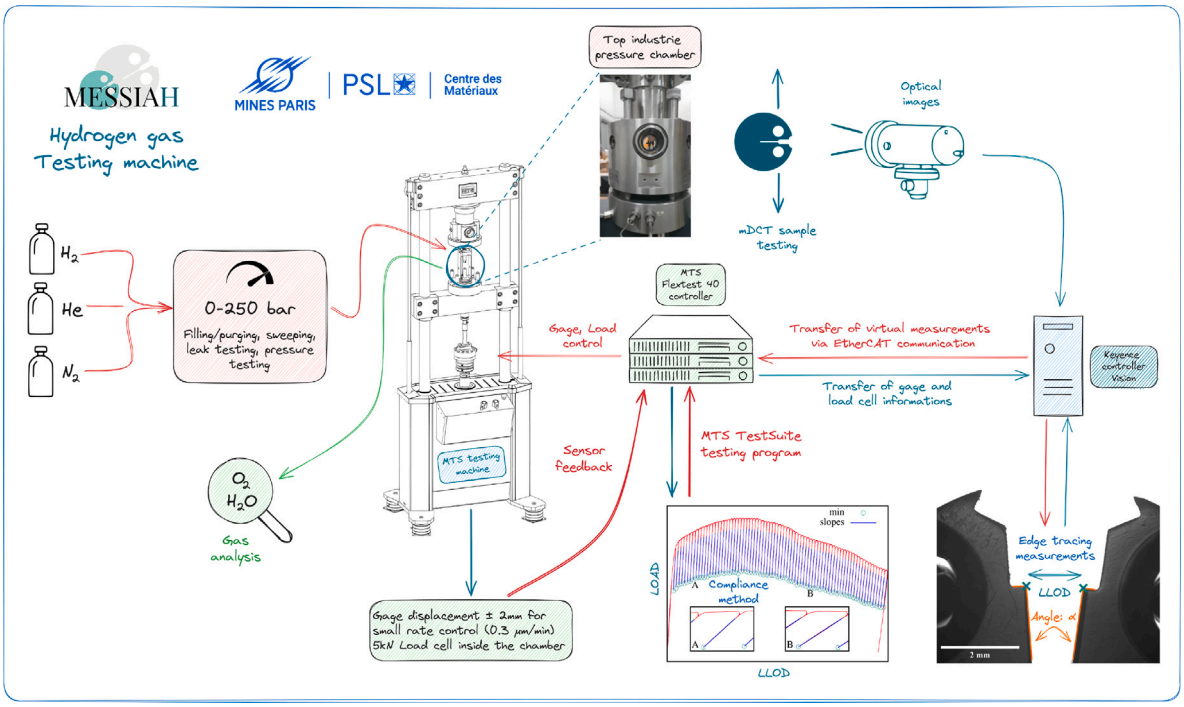

Fig. 1. Description of the test setup.

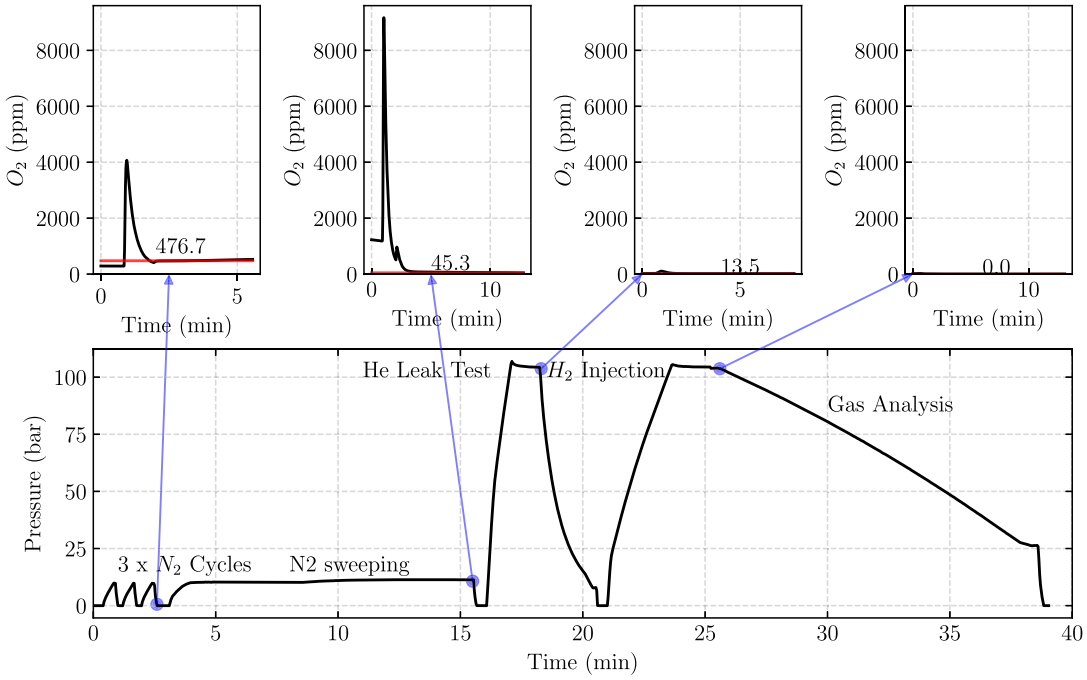

Fig. 2. Procedure for controlling gas impurities.

2.3. Test control using edge tracing (ET) technique

In hydrogen environment testing, the Edge Tracing (ET) technique is a preferred method for specimen analysis, offering high metrological accuracy and efficient image processing. This technique, unlike Digital Image Correlation (DIC) or marker tracking,

Table 1
Optical Engineering telecentric lenses used for sub-size specimens: fixed working distance of 132.4 mm.

Telecentric lens	Field of view (X*Y)	Calibration px/mm	Accuracy (%)
OE-TC-LWD 150	5.67 mm × 4.73 mm	435.17	0.05
OE-TC-LWD 100	8.50 mm × 7.09 mm	288.48	0.07
OE-TC-LWD 075	11.33 mm × 9.45 mm	215.29	0.53

Table 2
Chemical compositions of the E355 mod. steel grade.

	C	Mn	Si	Cr	Ni	Mo	S	P	Fe
At.%	0.15	1.38	0.19	0.04	0.02	0.01	0.002	0.015	Bal.

which require specimen surface alteration for tracking, preserves specimen integrity by avoiding any surface interaction with hydrogen environment. The method is suitable for identifying and tracking points, lines, and arcs along the edges of the specimen, ensuring comprehensive coverage and analysis. Its versatility lies in measuring varying distances between edges, crucial for monitoring radial contraction during tensile tests and assessing crack opening displacement (LLOD) for toughness measurements. In this study, the ET method is also employed to control the displacement speed in tensile tests by continuously monitoring radial contraction up to the point of rupture, and in toughness tests by tracking the rate of LLOD.

Telecentric lenses are used due to their ability to provide a clear image with a unique field of view (FOV), necessitated by the use of a pressurized chamber. These lenses not only simplify the setup process but also prevent edge distortion in the image, crucial for reducing potential measurement errors. Table 1 describes telecentric lenses suitable for sub-size specimens, used in conjunction with a 5 megapixels Keyence camera (LHR50). The optical system's calibration from pixels to millimeters is conducted using a cylindrical calibration pin, 2.4 mm in diameter, across the entire FOV. This calibration was further corroborated using a pin with a diameter of 1.050 mm. On the other hand, optical measurements provide precise access to the metrology of the sub-size specimens, as shown in Fig. 5-a. Due to their small dimensions, this metrology is very important for the analysis and interpretation of the tests. Table 1 also presents the accuracy error associated with each lens.

An unloaded specimen was monitored to assess the measurement fluctuation, with indicators such as low standard deviation pointing to reduced repeatability error. A comprehensive statistical analysis was conducted on the radial contraction of a tensile specimen using the OE-TC-LWD 150 lens. These results were compared with those obtained from a conventional clip mechanical extensometer, focusing on LLOD measurements. The analysis demonstrated that both extensometers exhibited low standard deviations, indicative of high precision: the optical method recorded a standard deviation of 0.28 μm in radial contraction measurements, while the mechanical sensor achieved marginally better performance with a standard deviation of 0.06 μm in LLOD measurements.

3. Material and geometries

The newly developed test setup underwent evaluation via a series of tensile and toughness tests in both ambient air and hydrogen environments. A comprehensive test campaign is designed to assess the performance and reliability of the apparatus, thereby offering insights into its efficacy for evaluating material properties under varied conditions.

This section is dedicated to present the studied material and specimen geometries.

3.1. Material

A modern E355 mod. (modified) steel grade, provided in the form of a hot rolled tube condition, is used in its as-received condition for this study. The tube features an internal diameter of 74.45 mm and a thickness of 12.7 mm. The chemical composition of the steel grade can be found in Table 2. The material exhibits a ferritic-pearlitic microstructure elongated in the L and T directions, as depicted in Fig. 3-a. Moreover, the steel grade's average inclusion volume fraction was determined as 0.065% through SEM observations. To assess the material's homogeneity, a microhardness profile was conducted with a 1 kg load and a dwell time of 10 s, using double staggered configuration. The results are illustrated in Fig. 3-b. Observations reveal the homogeneity of the material, with microhardness values ranging between 140 and 170 HV1. The average microhardness of the material is 153 HV1.

3.2. Specimen geometries

Fig. 4 depicts the various tensile specimen geometries employed in the research. The study began with the use of a macro standard tensile specimen, designated as ST-Φ_0 = 4 mm, featuring a diameter (Φ) of 4 mm and a gauge length (L_0) of 20 mm. This particular specimen served as a benchmark for validating the results obtained from the mini-specimens. Following this, two mini tensile specimens were introduced: the mST-Φ_0 = 2.4 mm, with a diameter (Φ) of 2.4 mm and a gauge length (L_0) of 4 mm, alongside its homothetic counterpart, the mST-Φ_0 = 1.2 mm, which possesses a diameter (Φ) of 1.2 mm and a gauge length (L_0) of 2 mm. All tensile specimens were extracted parallel to the longitudinal direction of the raw material. These miniaturized specimens were designed to facilitate a detailed analysis of material behavior under scaled-down dimensions. All tensile specimens were meticulously

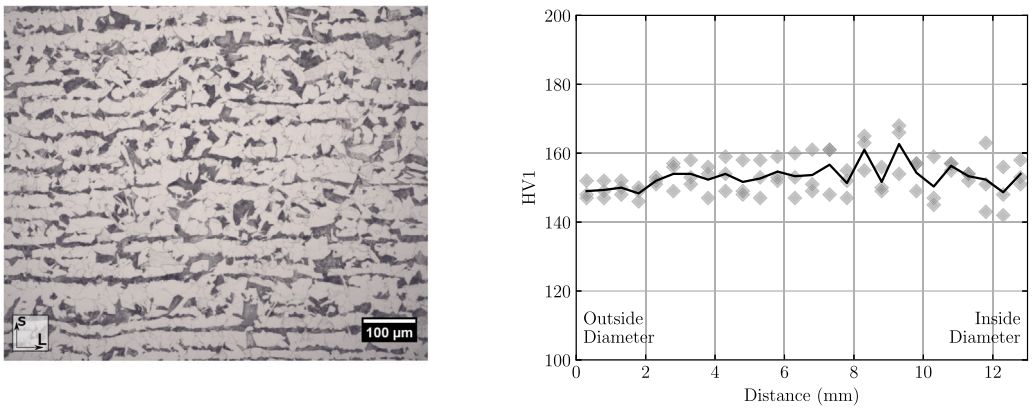

(a) Micrograph in the LS section (b) Microhardness profile through the thickness

Fig. 3. E355 mod. steel grade characterization.

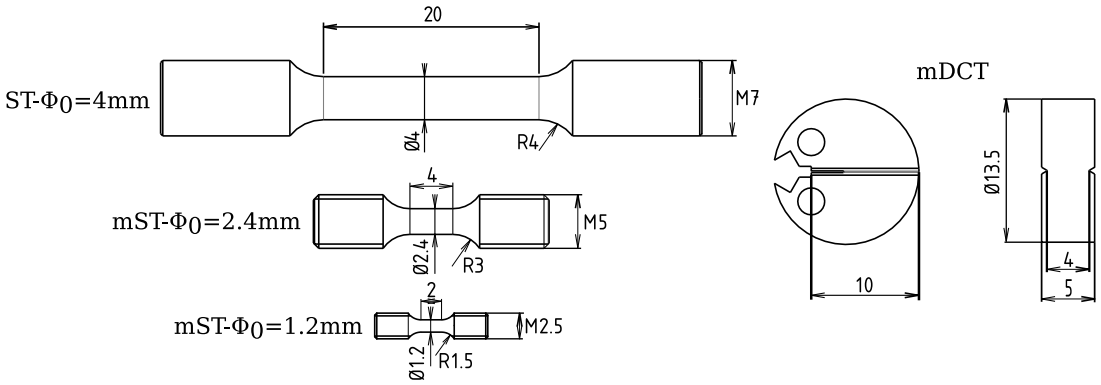

Fig. 4. Geometries of the specimens.

machined to maintain a surface roughness of 0.35 µm Ra, ensuring that the machining process did not adversely affect the residual stresses on the surface of the specimen.

Mini Disk-Shaped Compact Tension (mDCT) specimens with a 10 mm width (W) and 5 mm thickness (B) were machined without initial side grooves. These specimens were extracted in the LT direction. Surfaces were polished to 1 µm Ra to track fatigue pre-crack propagation according to ASTM E1820 guidelines. Final side grooves, ensuring a 4 mm net thickness (B_n), were added via EDM machining to promote a straight crack front, crucial for reliable fracture toughness testing.

4. Tensile tests on mini-specimens

This section aims to validate the testing methodology for sub-size specimens in ambient air, ensuring mini tensile specimens accurately represent material's mechanical properties. It also seeks to examine the effects of hydrogen on these specimens and validate the new test setup under gaseous H_2 environments.

4.1. Methodology

The primary objective is to ensure that mini tensile specimens accurately reflect the material's mechanical properties. This crucial step, conducted in ambient air, sets the foundation for subsequent evaluations in gaseous H_2 environments. To this end, a distinct experimental setup, as described in [24], is employed to compare specimens of varying sizes outlined in Fig. 4. Air tensile tests are conducted using an MTS hydraulic machine equipped with a 10 kN load cell, chosen to enhance measurement precision due to the smaller dimensions of the mini-specimens. The machine's crosshead displacement is regulated by an electromechanical extensometer (with a gauge length l_0) to maintain a strain rate of $5\times10^{-4}\ s^{-1}$. During testing, a camera, positioned perpendicularly to the specimen, captures images against a retro-illuminated white background from a LED panel. These images are then used to evaluate radial deformation using the Edge Tracing (ET) Technique.

Table 3
Coefficients of the constitutive law for the E355 mod. steel grade.

σ_0 (MPa)	Q_1 (MPa)	b_1	Q_2 (MPa)	b_2	Q_3 (MPa)
265	45	80	275	15	189

Following this, the tensile tests under H_2 are carried out using the machine setup detailed in Section 2.3. After the insertion of the specimen into the autoclave, the inertization procedure outlined in Section 2.2 is performed. At the conclusion of the inertization procedure, the autoclave is pressurized to a pressure over 50 bars higher than the desired pressure for the test. This step allows to conduct a gas analysis before the launching of the test, ensuring the effectiveness of the inertization. Following the gas analysis, a 60-minutes waiting period is observed to achieve the stabilization of the internal load cell. The ET technique, as detailed in Section 2.3, is employed to monitor the specimen deformation. Throughout the test, the minimal diameter of the specimen is tracked, enabling the determination of radial strain. Although the test is controlled by gauge displacement, a feedback loop has been programmed to adjust the displacement speed based on the virtual measurement. Radial contraction is used in order to maintain the quantity $\Delta\dot{\Phi}/\Phi_0 \times 2L_0 = \dot{\varepsilon} \times L_0$ constant, where L_0 corresponds to the gauge length of the specimen. The longitudinal strain rate is calculated at intervals of 10 μm of crosshead displacement. Fig. 5-a illustrates this principle applied to an mST specimen. The comparison with the displacement gauge shows that maintaining the speed in radial contraction implies a significant slowdown of the displacement gauge speed during the post-necking phase. All tests are performed under the strain rate of 5×10^{-4} s^{-1}. After concluding the test, a new gas analysis is performed to ensure that the low level of impurities was maintained throughout the test. The fracture surfaces of the specimens after the tensile tests are analyzed by means of field emission-SEM, operated at 15 kV.

4.2. Standard vs. mini-specimens: a ssessing size effect on mST

Fig. 5 displays the results obtained from the tests. In Fig. 5-b, the Engineering Stress (F/S_0) versus Engineering Strain ($\Delta l/l_0$) with overlay of True Stress–Strain curves graph up to the Ultimate Tensile Strength (UTS) shows considerable overlap among the three distinct specimens. However, Fig. 5-c reveals that the elongation at rupture, as measured from the crosshead displacement ($\Delta LL_p/L_0$), is significantly influenced by the dimensions of the specimens. Specifically, the post-necking elongation is observed to increase as the gauge length decreases: the ST-Φ_0 = 4 mm specimen has a L_0/Φ_0 ratio of 5, while the mST-Φ_0 = 2.4 mm and mST-Φ_0 = 1.2 mm specimens have a ratio of 1.66. This trend indicates that smaller gauge lengths result in greater post-necking elongation measurements. These observations align with prior studies [29,30] that observed similar effects. Zhao et al. through FEM analysis, attributed these effects to strain measurement inaccuracies during uniform elongation, stemming from machine compliance and deformation at the fillet region of the reduced section. Consequently, crosshead displacement measurements used for characterizing specimen ductility should be interpreted with caution.

Notably, reducing the diameter from 2.4 mm to 1.2 mm without altering the aspect ratio L_0/Φ_0 did not affect fracture elongation, diverging from the typical impact of thickness reduction on ductility observed in flat specimens [16,30–32]. Moreover, the consistent trend observed in the plot of F/S_0 against $\Delta\Phi/\Phi_0$ for all specimens, as depicted in Fig. 5-d, shows that local plastic behavior remains unaffected by specimen geometry and machining, even after the onset of post-necking. In this study, specimens were aligned with the rolling direction (L) for consistency. While anisotropic behavior is an important consideration for future research, [16,33], the isotropic deformation suggested by the fracture surfaces (Fig. 7) informs our current understanding.

4.3. Identification and validation of the plastic behavior

As it was demonstrated experimentally that plasticity is independent of specimen geometries, it is possible to determine a constitutive law for E355 mod. steel grade using the experimental data obtained from mini tensile specimens.

The determination of the constitutive law is performed using the Finite Elements Analysis (FEA) Z-set software,[1] [34]. The method uses the difference between experimental and finite element results as an objective function to be minimized. The fit of the hardening function is first done assuming von Mises plasticity. The fit is performed using the load–diameter reduction curves before the onset of sharp load drop. The flow stress σ_F is expressed as a function of the accumulated plastic strain p as:

$$\sigma_F(p) = \sigma_0 + Q_1(1 - \exp^{-b_1 p}) + Q_2(1 - \exp^{-b_2 p}) + Q_3 p \tag{2}$$

Here, σ_0 represents the yield stress, and the coefficients Q_1, b_1, Q_2, b_2, and Q_3 characterize the hardening law. These coefficients were optimized to minimize the objective function. The optimized coefficients are presented in Table 3. To enrich the analysis, the True Stress–Strain curve has been integrated, overlaying the experimental data with simulation outcomes for a direct comparison in Fig. 5-b. The concordance between experimental data and simulation results, particularly in the context of local plastic behavior shown in Fig. 5-d, indicates a high level of agreement, validating the established constitutive law for the E355 mod. steel grade.

[1] http://www.zset-software.com/

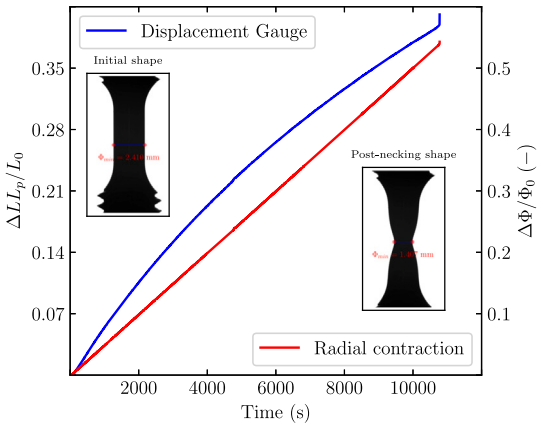

(a) Comparison of radial contraction and Gauge displacement over time. Example of metrology of mST specimen: inital shape and post-necking shape.

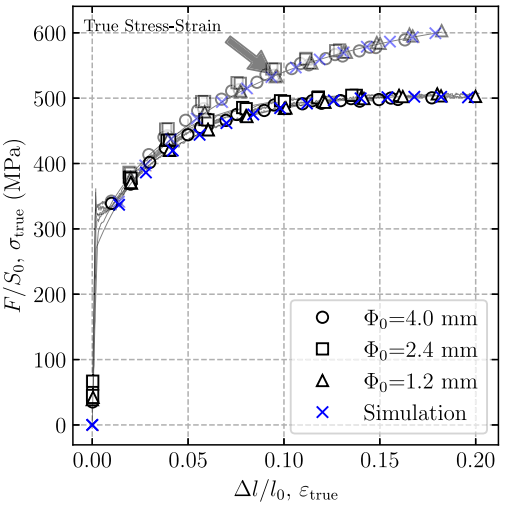

(b) $F/S_0 - \Delta l/l_0$ plot with overlay of True Stress-Strain curves.

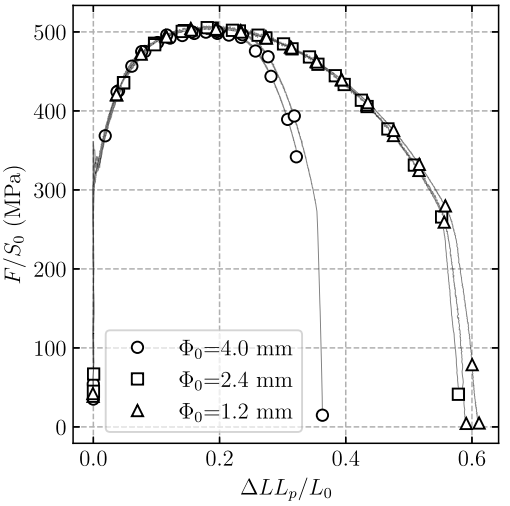

(c) $F/S_0 - \Delta LL_p/L_0$ plot.

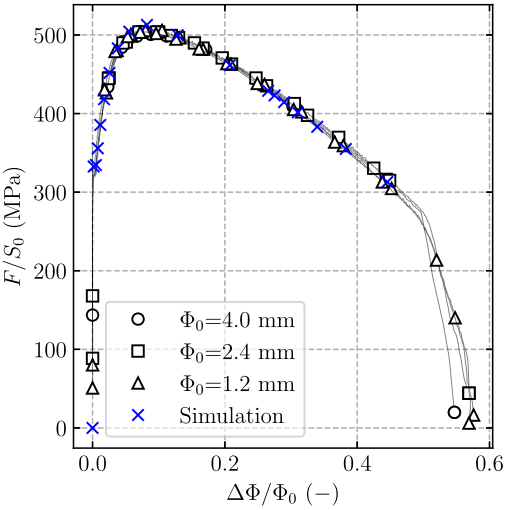

(d) $F/S_0 - \Delta\Phi/\Phi_0$ (−) plot.

Fig. 5. Methods and results of tensile testings conducted in air.

4.4. Hydrogen effect on mini tensile specimens

The results for mST-Φ_0 = 1.2 mm and mST-Φ_0 = 2.4 mm under different conditions, including air, 100 bar H_2, and 200 bar H_2, are depicted in Fig. 6. The results for mST-Φ_0 = 1.2 mm are represented with circles, while those for mST-Φ_0 = 2.4 mm with squares. Black markers correspond to results in air, gray to 100 bar H_2 and white to 200 bar H_2.

Table 4 presents a summary of the results.

As previously noted in Section 4, the results in air for both specimens are equivalent. Even with the strain rate of 5×10^{-4} s^{-1}, the impact of H_2 is evident in the results. Particularly in the decrease of the final elongation ($A = \Delta LL_p/L_0$) and the final radial strain ($Z = \Delta\Phi/\Phi_0$) when compared to the air results. These parameters can be exploited in order to calculate a Hydrogen Embrittlement Index based on final plastic elongation (HEI_A), according to Eq. (3):

$$HEI_A = \left(1 - \frac{A(H_2)}{A(Air)}\right) \times 100 \tag{3}$$

Table 4
Results of mST in air and in H_2.

Φ_0	Env.	Y.S. [MPa]	UTS [MPa]	A [%]	Z [%]	HEI_A [%]	HEI_Z [%]
1.2 mm	Air	301	506	58.2	56.2		
	100 bar H_2	316	502	40.0	28.0	31.2	50.2
	200 bar H_2	338	501	36.6	22.9	37.1	59.2
2.4 mm	Air	320	506	57.9	56.9		
	100 bar H_2	333	508	47.7	33.4	17.6	41.3
	200 bar H_2	341	501	40.1	26.1	29.5	54.1

and one based on final radial strain (HEI_Z), according to Eq. (4):

$$HEI_Z = \left(1 - \frac{Z(H_2)}{Z(Air)}\right) \times 100 \tag{4}$$

Hydrogen embrittlement is observed in the tests conducted with H_2, resulting in a HEI_A ranging between 17.6% and 37.1% and a HEI_Z ranging between 41.3% and 59.2%. The increase in H_2 pressure leads to more pronounced embrittlement. For mST-Φ_0 = 1.2 mm HEI_Z increases from 50.2% to 59.2% as the H_2 pressure rises from 100 to 200 bar, while for mST-Φ_0 = 2.4 mm it increases from 41.3% to 54.1% for 100 and 200 bar H_2, respectively. Additionally, the influence of specimen geometry on H_2 embrittlement is noticeable. The mST-Φ_0 = 1.2 mm exhibits higher embrittlement than the mST-Φ_0=2.4 mm under the same H_2 pressure. For instance, HEI_Z at 100 bar H_2 is 50.2% for mST-Φ_0 = 1.2 mm and 41.3% for mST-Φ_0 = 2.4 mm. This effect seems to be associated with the H_2 diffusion, as hydrogen can penetrate relatively deeper in the mST-Φ_0 = 1.2 mm specimen, resulting in a larger embrittlement.

In order to illustrate the difference in hydrogen diffusion within both specimens, a simple comparison using Fick's Equations is proposed. To calculate the depth of hydrogen penetration into the material, Eq. (5) can be utilized:

$$l = \sqrt{Dt} \tag{5}$$

Where l is the penetration depth, D is the Diffusion Coefficient and t indicates time. Considering $D = 1.27 \times 10^{-8}$ m^2/s, [35], the time required to hydrogen penetrate the mST-Φ_0-1.2 mm specimen to its center (i.e. l = 0.6 mm) is 28 s, while for mST-Φ_0 = 2.4 mm (l = 1.2 mm), it is 113 s. This implies that hydrogen penetration into the mST-Φ_0 = 2.4 mm specimen takes four times longer compared to its penetration into the mST-Φ_0 = 1.2 mm specimen. However, a more precise analysis of hydrogen diffusion necessitates a model incorporating additional factors such as the stress field and hydrogen trapping by dislocations, as proposed by Pinto et al. [35].

HEI_Z results in values higher than those derived from HEI_A. Indeed, HEI_Z is directly related to necking, which represents a localized deformation in the fracture zone, whereas HEI_A correlates with the average axial deformation, which is influenced by the specimen's gauge length. Based on these results, HEI_Z is considered more sensitive and thus more effective for evaluating hydrogen embrittlement (HE) susceptibility. This finding is in agreement with the conclusions presented by Du et al. [12].

The results obtained in this work are in accordance with results from others authors [36–38]. Briottet et al. [36] performed tensile tests under 300 bar H_2. They observed that Hydrogen did not affect the YS and the UTS. Furthermore, they obtained HEI_A between 38.3% and 60.9% for strain rates ranging between 2×10^{-6} s^{-1} and 5×10^{-5} s^{-1}. Michler et al. [37] found more severe HE for higher H_2 pressure in tensile tests. Nanninga et al. [38] did the comparison of gaseous hydrogen embrittlement of three pipeline steels. Similarly, they have found that gaseous hydrogen did not have significant effect on YS and UTS, but the ductility of the studied steel was reduced.

4.5. Fractography

Fig. 7 displays the fracture surfaces of the mST-Φ_0 = 1.2 mm specimens tested under air, 100 bar H_2, and 200 bar H_2. Figs. 7a–c depict the lateral views of the specimens. The higher ductility of the specimen tested under air is noticeable, as evidenced by significant necking during the test. In contrast, there is a lower area reduction observed in the specimens tested under H_2. Furthermore, the substantial quantity of secondary cracks observed in the specimens tested under H_2 is noteworthy.

Figs. 7d–f illustrate the top views of the specimens. In Fig. 7-d, the predominance of Micro Void Coalescence (MVC) is evident in the specimen tested under air. Different features are observed in the fracture surfaces of the specimens tested under H_2.

Fig. 7-g provides a higher magnification view of the specimen tested under 100 bar H_2. A predominance of Quasi-Cleavage (QC) fracture aspect is observed near the surface, with a smooth transition to MVC in the center. However, the dimples found in this specimens are smaller than those observed in the specimen tested under air.

Fig. 7-h offers a higher magnification of the specimen tested under 200 bar H_2. An almost exclusive predominance of Quasi-Cleavage (QC) fracture aspect is seen from the surface to the center of the specimen. However, small dimples are found in the center of the specimen, and these dimples are smaller than the ones observed in the specimen tested under 100 bar H_2.

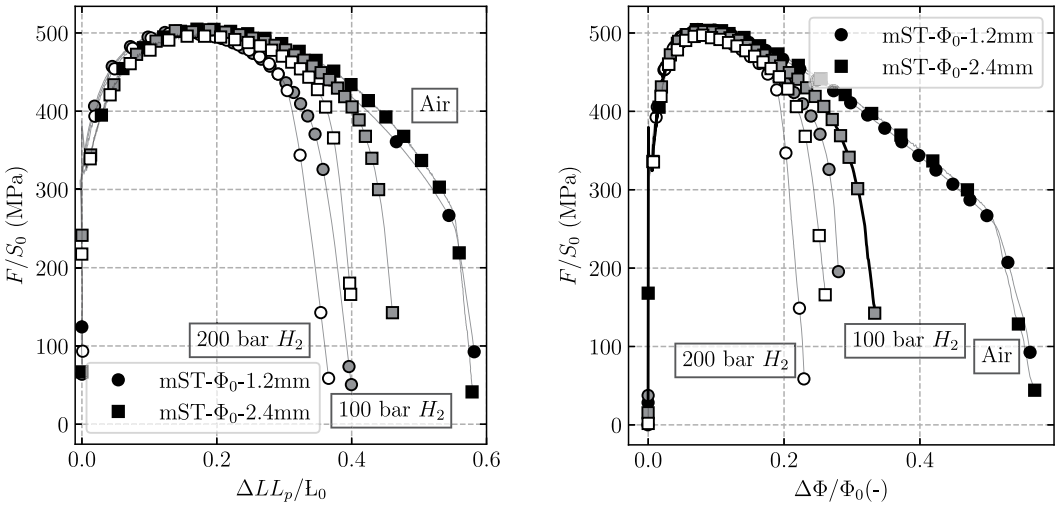

(a): $F/S_0 - \Delta LL_p/L_0$ plot. (b): $F/S_0 - \Delta\Phi/\Phi_0(-)$ plot.

Fig. 6. Results for mST-Φ_0 = 1.2 mm and mST-Φ_0 = 2.4 mm under air, 100 bar H_2, and 200 bar H_2.

5. Toughness test on mini-specimens

Having validated the tensile testing methodology with mini-specimens, the subsequent step is to extend this approach to toughness tests. This progression aims to contribute to a more comprehensive understanding of material behavior under varying conditions.

5.1. Methodology

5.1.1. Pre-cracking

The mDCT specimens are first machined without side grooves. Subsequently, the sides of each specimen are polished until 1 μm Ra to facilitate the tracking of crack propagation using an optical device. Precracking of the specimens is performed using an electromechanical Instron Electropuls E10000 Linear-Torsion machine with a force capacity of +/- 10,000 N. Due to the reduced size of the mDCT specimen, special attention is given to the precracking procedure to avoid its influence on subsequent results. Initially, a K_{max} of 15 MPa$\sqrt{m}$ was applied, with a ratio load (R) of 0.1 and frequency (f) of 35 Hz. Every 30,000 cycles, the fatigue procedure is halted to measure crack advancement on the polished sides of the specimen. Subsequently, the force is adjusted to maintain the initial K_{max} of 15 MPa$\sqrt{m}$. During each interruption, the specimen is rotated to mitigate any effects of misalignment of the load line on crack propagation. This initial load is sustained until reaching half of the desired precrack propagation. Following this, each 30,000 cycles, the load is reduced to achieve a K_{max} of approximately 12 MPa$\sqrt{m}$ at the end of the fatigue precrack procedure. This procedure results in a theoretically calculated plastic zone radius of around 0.125 mm, representing approximately 2.5% of the original remaining ligament (b_0). The total number of cycles requires to achieve a precrack propagation of around $a_0/W = 0.5$ ranged between 210,000 and 250,000. After this procedures, the side grooves are EDM machined.

5.1.2. Compliance method

The machine setup detailed in Section 2.3 is used for conducting a toughness test on the mDCT specimen. The Edge Trace Technique is employed to monitor key parameters, including Load Line Opening Displacement (LLOD) and the Opening Angle (α).

To assess crack propagation during the test, the elastic compliance method is employed, involving a loading/holding/unloading procedure. During the loading step, a displacement is applied at a LLOD rate of 100 μm/min until reaching an incremental load line displacement of 50 μm. Subsequently, the displacement is maintained for a holding time of 30 s to prevent material relaxation during the unloading and loading steps. Following the holding time, the specimen is unloaded to 65% of the charge that is reached at the end of the holding step and reloaded to the this same force. This step enables the calculation of the crack length using the compliance equations available in ASTM E1820. This sequence is repeated until a significant crack propagation of approximately 1.3–1.5 mm is achieved. After completing the last cycle, the force is returned to zero.

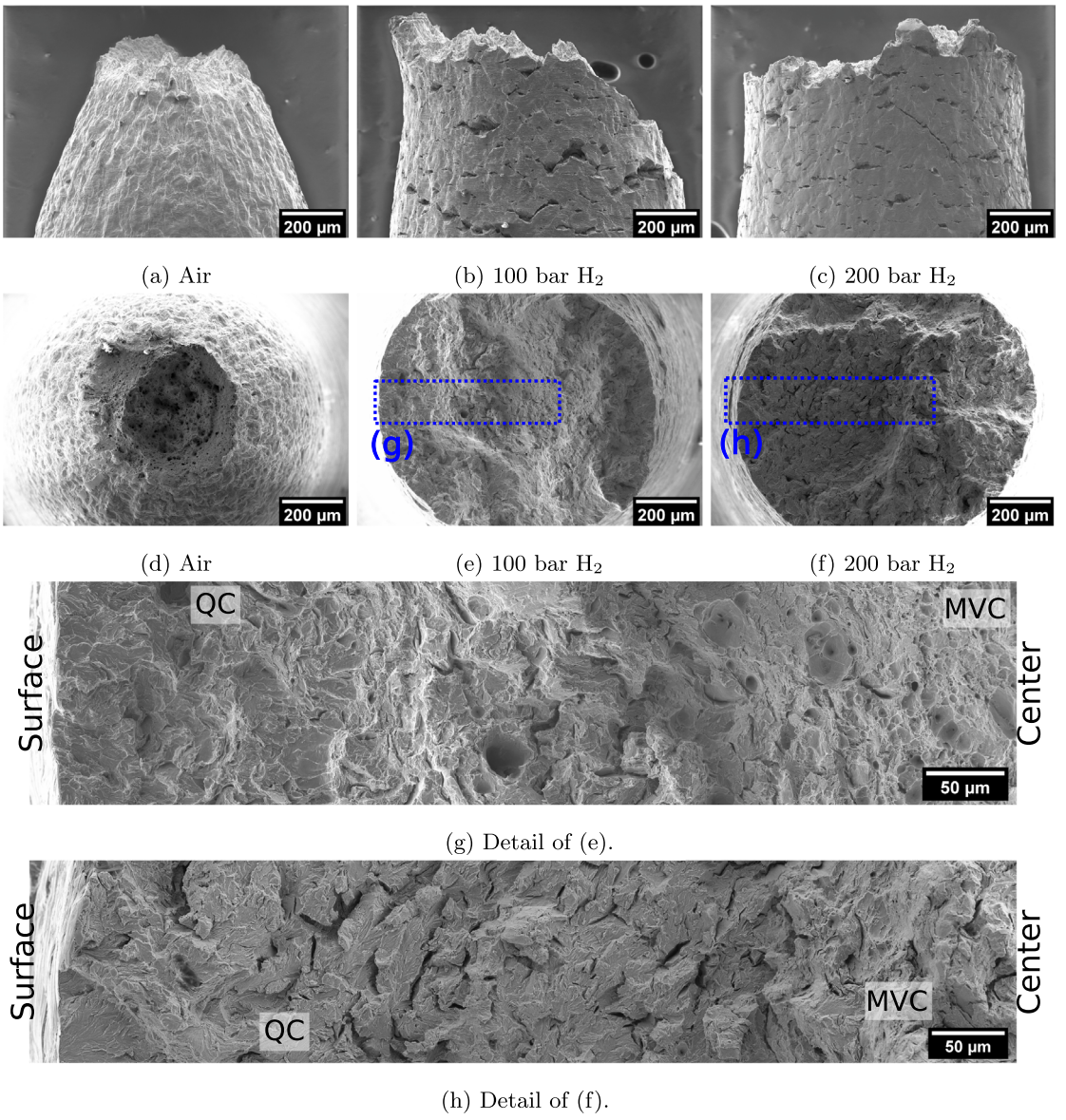

Fig. 7. Fracture surfaces of the mST-Φ_0 = 1.2 mm specimens tested under air, 100 bar H_2 and 200 bar H_2.

5.1.3. CTOD determination

Crack Tip Opening Displacement (CTOD — δ) can be measured using the double clip gauge method, where a pair of clip gauges are mounted above the notch. These clip gauges measure the Crack Mouth Opening Displacement (CMOD) at different heights above the specimen crack mouth, enabling the determination of δ through geometric considerations. This methodology has been applied by various authors [39–42].

In this work, a methodology is proposed, based on the double-clip gauge method developed by ExxonMobil [43]. However, instead of employing two clip gauges, the CTOD is calculated based on the Load Line Opening Displacement (LLOD) and the Opening Angle (α), which can be directly measured using ET technique. Fig. 8-a shows a schematic representation of the specimen during the test, where δ is the CTOD measured at the 90° intersect starting from the original crack tip and a_0 is the initial crack length. Based on geometric and trigonometric assumptions, it is possible to obtain the following:

$$\sin\left(\frac{\alpha}{2}\right) = \frac{\mathrm{LLOD} - \delta}{2a_0} \tag{6}$$

Subsequently, it is possible to isolate δ, leading to the following:

$$\delta = \mathrm{LLOD} - 2a_0 \sin\left(\frac{\alpha}{2}\right) \tag{7}$$

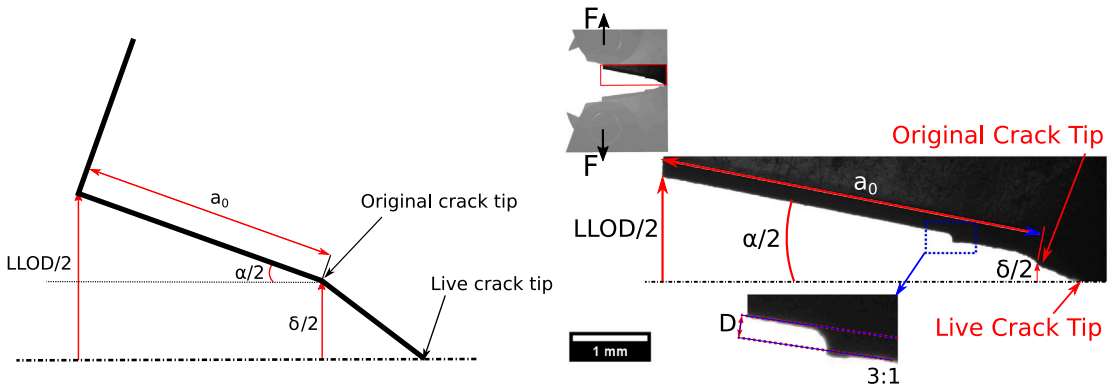

(a) Schematic representation of LLOD, Opening Angle (α) and CTOD (δ).

(b) Extraction of CTOD (δ) from ET technique

Fig. 8. Schematic representation to measure CTOD (δ) using ET technique.

Fig. 8-b presents an excerpt from an image captured during a toughness test. The measurements required to compute δ are indicated in the image. It is noticeable that LLOD is measured at the edge of the starter notch, resulting in an offset (D) relative to the fatigue crack. Despite the small value (approximately 0.075 mm) of this offset, it is considered in the calculation of LLOD in Eq. (7), imposing a LLOD correction of $-2D(1-\cos(\alpha/2))$. This offset is not depicted in Fig. 8-a to enhance the clarity of the image. Eq. (7) thus becomes:

$$\delta = \mathrm{LLOD} - 2D(1-\cos\frac{\alpha}{2}) - 2a_0\sin(\frac{\alpha}{2}) \tag{8}$$

After the conclusion of each test, a post-test fatigue cycling is performed to mark the crack extension. The crack extension as well as the fatigue pre-crack are measured using the nine points average procedure based on optical measurements.

The mDCT specimens tested under H_2 follow the same procedure outlined above. Similarly to what is presented in Section 4.4, the gas analysis is performed both before and after the test to verify the low content of impurities.

5.2. Results in air

Fig. 9 illustrates the results obtained for an mDCT specimen tested in an air atmosphere. The experimental data Load − LLOD is represented in Fig. 9-a. Additionally, Fig. 9-b presents the $J-\Delta a$ curve obtained from this specimen. The experimental points are marked with black triangles. The J_Q value exceeding the $J_{\max}$ suggests the test is not valid according to the ASTM E1820 standard.

The evolution of δ during crack propagation is illustrated in Fig. 9-c. For comparison, δ calculated according to the ASTM E1820 standard (δ_{ASTM}) is presented in the graph. As observed, δ_{ASTM} yields more conservative δ values, a point previously discussed by other authors [41]. δ and δ_{ASTM} values were compared with an estimated actual δ measured in a post-mortem specimen. Before undergoing the post-fatigue procedure, the specimen was measured using an optical profilometer, observing δ from the lateral of the specimen. The analysis revealed that δ calculated is 9.8% higher than the estimated actual δ, whereas the δ_{ASTM} is 46% lower. Specifically, δ and δ_{ASTM} demonstrate a better correlation below the $\delta_{\mathrm{ASTMmax}}$, as illustrated in Fig. 9-c. However, beyond this threshold, the deviation between δ and δ_{ASTM} becomes more pronounced. It is acknowledged that the relationship between δ and J is no longer valid under conditions of excessive plasticity or significant crack growth. This limitation arises because J-Integral concept is applicable when the plastic zone is small relative to the overall dimensions of the specimen [44,45]. The maximum force is indicated in Fig. 9-a as a red dot, and δ at maximum force (δ_m) is marked in Fig. 9-c also as a red dot. The value of δ_m is 0.48 mm, higher than the 0.40 mm $\delta_{\mathrm{ASTM_Q}}$ calculated according to the ASTM E1820 standard and denoted as a red square. This 20% difference emphasizes the fact that ASTM E1820 calculation of δ results in lower values. However, it is essential to note that 0.40 mm does not represent a valid critical δ, as this value exceeds the 0.23 mm $\delta_{\mathrm{ASTM_{max}}}$ calculated according to the ASTM E1820 standard.

5.3. Results in hydrogen

Fig. 10 illustrates the $J-\Delta$a curves obtained for mDCT specimens under different conditions: air, 100 bar H_2, and 200 bar H_2. The obtained J_Q or J_{IC} values are displayed as red points in the plot.

Table 5 provides a summary of the results.

It can be observed the effect of H_2 pressure on toughness specimen. Increasing H_2 pressure from 100 bar to 200 bar resulted in a decrease in J_Q value from 238.7 MPa$\sqrt{\mathrm{m}}$ to 140.3 MPa$\sqrt{\mathrm{m}}$. Similarly to the HEI_Z presented in Section 4.4, HEI_{J_Q} can be defined using the Eq. (9):

$$\mathrm{HEI}_{J_Q} = \left(1 - \frac{J_Q(\mathrm{H_2})}{J_Q(\mathrm{Air})}\right) \times 100 \tag{9}$$

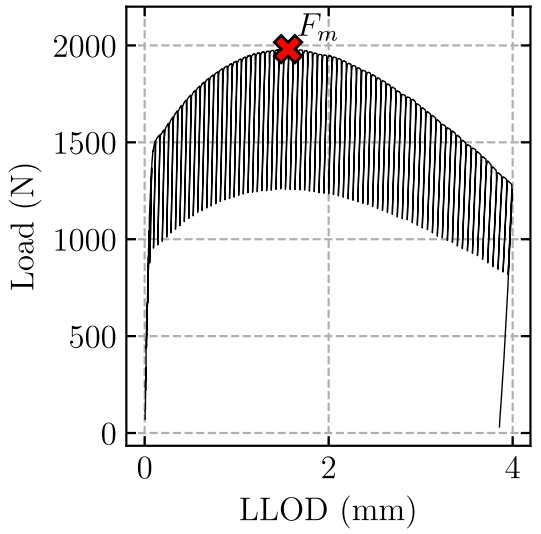

(a) Load − LLOD plot.

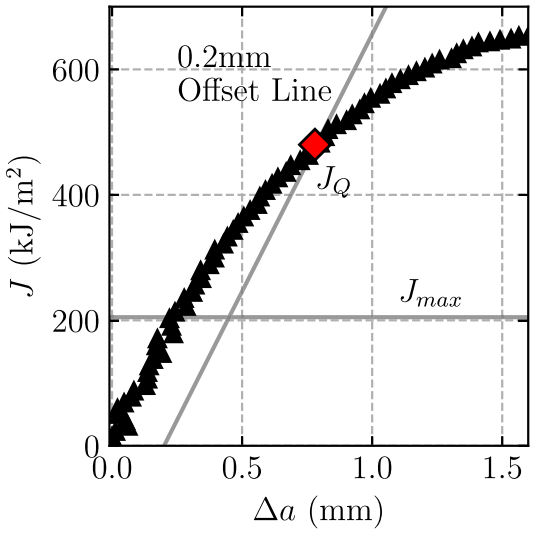

(b) $J - \Delta a$ plot.

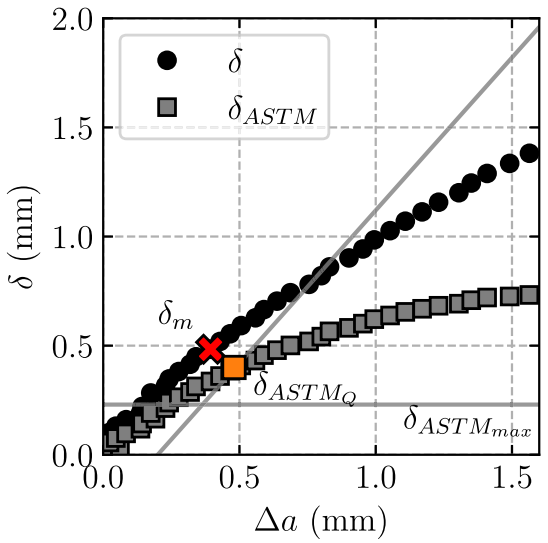

(c) $\delta - \Delta a$ plot.

Fig. 9. Results obtained for a mDCT specimen tested in an air atmosphere.

Notably, significant HEI_{J_Q} was observed with 100 bar H_2 and 200 bar H_2: 47.5% and 81.8%, respectively.

Fig. 10-b also shows the evolution of δ during crack propagation. Similarly, the influence of H_2 pressure on specimen toughness is evident through the decrease in δ_m with increasing test pressure. The tests under air and under 100 bar H_2 presented similar values of δ_m : 0.48 mm and 0.43 mm, respectively. In contrast, the test conducted under 200 bar H_2 presented a δ_m of 0.02 mm, representing a notably low δ. A remark should be made regarding the plot $\delta - \Delta a$ of the test under 200 bar H_2. As observed, two points are highlighted: δ_m marked with red 'x' in red and δ_C marked with orange '+'. The reason behind this distinction is elucidated in the F−LLOD plot (Fig. 10-c). The orange '+' point corresponds to the first local maximum force, while the red point represents the global maximum force of the test. The same colors were used in the $\delta - \Delta a$ plot (Fig. 10-b). In this study, it is assumed that δ associated with the initiation of crack propagation is linked with the first local maximum force (orange point '+'). This implies that crack propagation occurs with minimal crack blunting, what is confirmed in the SEM image in Fig. 11-g. Consequently, it means

Table 5
Results of mDCT in air and in H_2.

Env	a_0 [mm]	a_f [mm]	J_Q, J_{IC} [kJ/m^2]	K_{J_Q}, $K_{J_{IC}}$ [MPa$\sqrt{m}$]	δ_m [mm]	HEI_{J_Q} [%]	HEI_{δ_m} [%]
Air	5.20	7.02	493.4	329.3	0.48		
100 bar H_2	5.19	6.76	259.2	238.7	0.43	47.5	10.42
200 bar H_2	5.20	7.12	89.6	140.3	0.02	81.8	95.83

that the experimental data must be interpreted with caution. Misinterpretation could potentially result in less conservative values for δ.

A Hydrogen Embrittlement Index can be calculated based on the δ_m value (HEI_{δ_m}, Eq. (10)):

$$HEI_{\delta_m} = \left(1 - \frac{\delta_m(H_2)}{\delta_m(Air)}\right) \times 100 \tag{10}$$

The calculated HEI_{δ_m} values are presented in Table 5. HEI_{δ_m} observed for 100 bar H_2 is 10.42%, a value not so high as the 47.5% seen for HEI_{J_Q} in the same test. However, the test under 200 bar H_2 revealed a HEI_{δ_m} of 95.83%, even more severe than the 81.8% HEI_{J_Q} for the same test. These results highlight the contrasts that can arise in different Hydrogen Embrittlement Index criteria, even when considering similar test methodologies. In this case, a $J - \Delta a$ and a $\delta - \Delta a$ curves are extracted from the same test.

The existing body of literature offers limited references for direct comparison with our results. However, it is recognized that hydrogen embrittlement tends to increase with increasing hydrogen gas pressure [46]. Briottet et al. [36] performed fracture toughness measurements in air and in 300 bar H_2 on X80 steel. They observed a decrease of the toughness of this alloy from 210 kJ/m^2 in air to 15 kJ/m^2 in H_2, representing around 92.8% of decrease in toughness, what is reasonable in comparison with 81.8% obtained in this work for 200 bar H_2. Wang et al. [47] presented a quantitative model to predict the fracture toughness of steels in gaseous hydrogen. The model was validated with experimental data [48,49], obtaining good agreement. The study shows the decreasing of toughness properties with the increasing of hydrogen pressure.

5.4. Fractography

The fracture surfaces of the specimens after the toughness tests were analyzed by means of field emission-SEM, operated at 15 kV.

Fig. 11 depicts the fracture surfaces of the mDCT specimens tested under air (Figs. 11a–c), 100 bar H_2 (Figs. 11d–f), and 200 bar H_2 (Figs. 11g–i).

The fracture surface of the specimen tested under air (Figs. 11a–c) exhibits the typical ductile behavior. In Fig. 11b, the characteristic zones of pre-crack, blunting, and propagation are clearly visible. The propagation zone, highlighted in Fig. 11-c, reveals the presence of MVC. For mDCT specimen tested under 100 bar H_2, the blunting zone is similarly observed (Fig. 11-e). However, in Fig. 11-f, the initiation of crack propagation displays a mixed mode of fracture, featuring both MVC and QC. In contrast, the mDCT specimen tested under 200 bar H_2 does not exhibit a blunting zone, as shown in Fig. 11-h. Instead, a direct transition is observed from the pre-crack to the propagation zone. Furthermore, the onset of the propagation zone presents a distinctly brittle appearance, characterized by quasi-cleavage (QC) fracture, as illustrated in Fig. 11-i. This observation aligns with findings by Ogawa et al. [50], who reported similar behavior in carbon steel tested in 115 MPa hydrogen gas. In their study, the crack propagated with the formation of QC, maintaining a sharp, minimally blunted shape.

6. Conclusions and remarks

This paper presents a methodology that employs sub-size specimens with an innovative setup for a specialized gaseous pressurized hydrogen tensile machine. An optical extensometer employing Edge Tracing (ET) technique was developed to measure local specimen strain and control machine displacement during mechanical tests. The application of this methodology was demonstrated on a modern ferrito-pearlitic material, leading to the following conclusions:

- The developed methodology successfully yields reliable results in tensile tests with mini-specimens. The local measurement of radial strain is an effective way of comparing the results of samples of different sizes. Additionally, a constitutive law could be established using mini-specimens.
- Toughness tests with mini-specimens, monitoring LLOD and the opening angle through ET, allow the determination of $J - \Delta a$ and $\delta - \Delta a$ plots. Due to the high toughness and small dimensions of the specimen, J_Q value obtained is not valid according to the ASTM E1820 standard. It is observed that δ_{ASTM_Q}, calculated by J conversion according to ASTM E1820, yields a more conservative value (0.40 mm) compared to the δ_m of 0.48 mm, determined from ET technique.
- Tensile tests conducted under varying H_2 pressures reveal significant insights into the Hydrogen Embrittlement effect. The HEI_A and HEI_Z indexes show the influence of H_2 pressure and specimen size on embrittlement. Notably, HEI_Z, reflecting localized strain, yields less conservative but more suitable values for assessing Hydrogen Embrittlement, as evidenced by the differing results obtained for mST specimens with diameters of 1.2 mm and 2.4 mm under different H_2 pressures.

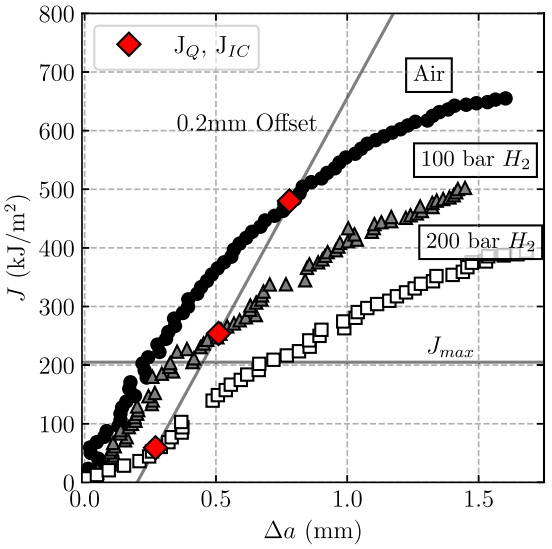

(a) $J - \Delta a$ plot.

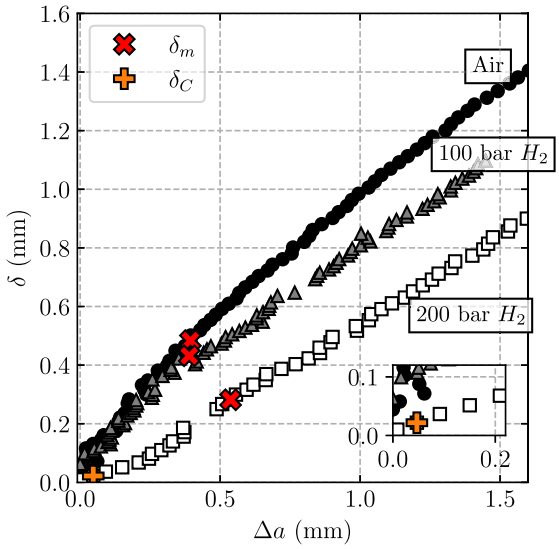

(b) $\delta - \Delta a$ plot.

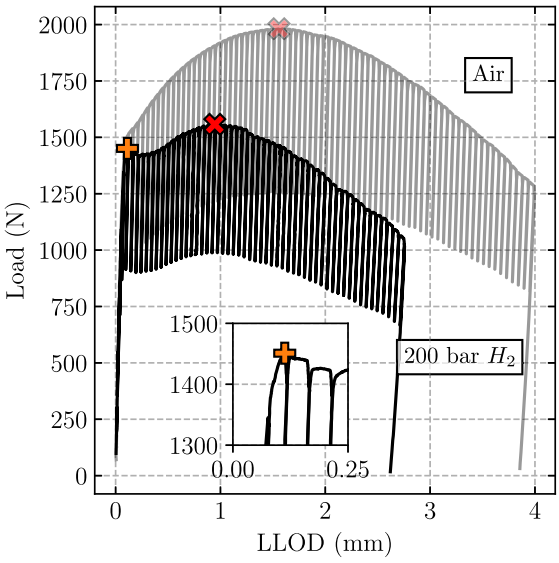

(c) Load − LLOD plot.

Fig. 10. Toughness results obtained for mDCT specimens under different environments.

- The impact of different H_2 pressures on toughness was quantified through HEI_{J_Q} and $HEI_{\delta m}$ indexes. The results showed a HEI_{J_Q} of 47.5% and 81.8% for 100 bar H_2 and 200 bar H_2, respectively, and HEI_{δ_m} values of 10.42% and 95.8% for the same pressures. Particularly, the test at 200 bar H_2 demonstrated no blunting before crack propagation, underscoring the critical role of fracture observation in assessing hydrogen embrittlement and the need for detailed analysis. It is important to emphasize that the reported hydrogen embrittlement index values are derived from a single test per configuration, implying that while they provide valuable insights into the effects under specific conditions, broader generalizations from these results require additional testing across varied conditions.

The approach outlined in this paper provides a foundational basis for investigating a diverse array of materials by extracting small coupons. This includes studying heterogeneous materials, different weld zones, components with low thickness, precious materials,

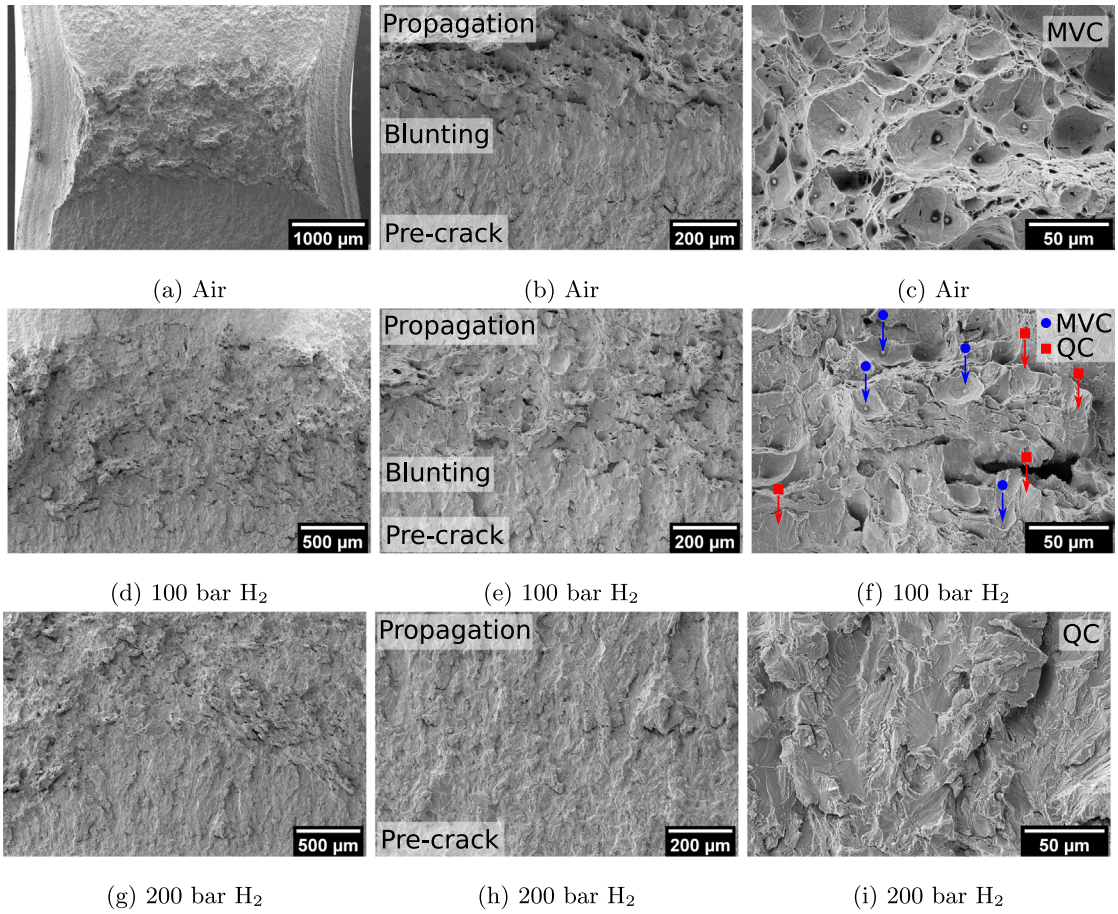

Fig. 11. Fracture surfaces of the mDCT specimens tested under air, 100 bar H_2 and 200 bar H_2.

deposited layers, and monitoring installations. This research importantly contributes to the expanding focus on adapting current pipeline networks for the transportation of hydrogen, a field that is attracting international attention.

CRediT authorship contribution statement

Y. Madi: Writing – review & editing, Writing – original draft, Visualization, Validation, Supervision, Software, Resources, Project administration, Methodology, Investigation, Formal analysis, Data curation, Conceptualization. **L.M. Santana:** Writing – review & editing Writing – original draft, Visualization, Validation, Methodology, Investigation, Formal analysis, Data curation, Conceptualization. **S. Belkacemi:** Writing – review & editing, Methodology, Investigation, Data curation. **V. Farrugia:** Writing – review & editing, Methodology, Investigation. **A. Meddour:** Writing – review & editing, Resources, Methodology, Investigation. **P-J. Marchais:** Writing – review & editing, Validation, Resources, Methodology, Funding acquisition. **M. Bertin:** Writing – review & editing, Validation, Resources, Methodology, Funding acquisition. **J. Furtado:** Writing – review & editing, Validation, Resources, Methodology, Investigation, Funding acquisition.

Declaration of competing interest

The authors declare that they have no known competing financial interests or personal relationships that could have appeared to influence the work reported in this paper.

Data availability

Data will be made available on request.

Acknowledgments

This research was supported by the ANR Chair program MESSIAH (ANR-20-CHIN-0003, MESSIAH for Mini-tests for In-Service Monitoring of Structures with Application to Hydrogen Transport). We extend our gratitude to Emerick Lenud for his valuable contribution during his internship, particularly in implementing the optical measurement technique on the testing machine. We extend our sincere thanks to Jacques Besson for his invaluable analysis and commentaries to this technical paper. We also acknowledge the SESAME and JPE platforms of Centre des Matériaux, MINES Paris for their significant roles in developing the testing machine and refining the machining process of the mini-specimens.

References

[1] European Hydrogen Backbone, A European hydrogen infrastructure vision covering 28 countries, 2022, https://ehb.eu/files/downloads/ehb-report-220428-17h00-interactive-1.pdf. (Accessed: January 6 2024), at 15:00.
[2] L. Zemite, L. Jansons, N. Zeltins, S. Lappuke, I. Bode, Blending hydrogen with natural gas/biomethane and transportation in existing gas networks, Latvian J. Phys. Techn. Sci. 60 (5) (2023) 43–55, http://dx.doi.org/10.2478/lpts-2023-0030.
[3] S. Lynch, Hydrogen embrittlement phenomena and mechanisms, Corros. Rev. 30 (3–4) (2012) 105–123, http://dx.doi.org/10.1515/corrrev-2012-0502.
[4] M.B. Djukic, G.M. Bakic, V. Sijacki Zeravcic, A. Sedmak, B. Rajicic, The synergistic action and interplay of hydrogen embrittlement mechanisms in steels and iron: Localized plasticity and decohesion, Eng. Fract. Mech. 216 (2019) 106528, http://dx.doi.org/10.1016/j.engfracmech.2019.106528.
[5] A. Laureys, R. Depraetere, M. Cauwels, T. Depover, S. Hertelé, K. Verbeken, Use of existing steel pipeline infrastructure for gaseous hydrogen storage and transport: A review of factors affecting hydrogen induced degradation, J. Natural Gas Sci. Eng. 101 (2022) 104534, http://dx.doi.org/10.1016/j.jngse.2022.104534.
[6] J. Hoschke, M.F.W. Chowdhury, J. Venezuela, A. Atrens, A review of hydrogen embrittlement in gas transmission pipeline steels, Corros. Rev. 41 (3) (2023) 277–317, http://dx.doi.org/10.1515/corrrev-2022-0052.
[7] A. Campari, F. Ustolin, A. Alvaro, N. Paltrinieri, A review on hydrogen embrittlement and risk-based inspection of hydrogen technologies, Int. J. Hydrogen Energy 48 (90) (2023) 35316–35346, http://dx.doi.org/10.1016/j.ijhydene.2023.05.293.
[8] M.A. Kappes, T.E. Perez, Blending hydrogen in existing natural gas pipelines: Integrity consequences from a fitness for service perspective, J. Pipeline Sci. Eng. 3 (4) (2023) 100141, http://dx.doi.org/10.1016/j.jpse.2023.100141.
[9] T. Matsuo, J. Yamabe, H. Furukawa, K. Seki, K. Shimizu, S. Watanabe, S. Matsuoka, Development of new strain gage for high-pressure hydrogen gas use, Exp. Mech. 54 (3) (2014) 431–442, http://dx.doi.org/10.1007/s11340-013-9816-4.
[10] B. Somerday, J. Campbell, K. Lee, J. Ronevich, C. San Marchi, Enhancing safety of hydrogen containment components through materials testing under in-service conditions, Int. J. Hydrogen Energy 42 (11) (2017) 7314–7321, http://dx.doi.org/10.1016/j.ijhydene.2016.04.189, Special issue on The 6th International Conference on Hydrogen Safety (ICHS 2015), 19-21 October 2015, Yokohama, Japan.
[11] T. Ogata, Evaluation of hydrogen embrittlement by internal high pressure hydrogen environment in specimen, J. Japan Inst. Metals 72 (2) (2008) 125–131, http://dx.doi.org/10.2320/jinstmet.72.125.
[12] J. Du, H. Ming, J. Wang, E.-H. Han, Hydrogen embrittlement of 20 seamless steel in medium and low pressure gaseous hydrogen, Mater. Lett. 334 (2023) 133734, http://dx.doi.org/10.1016/j.matlet.2022.133734.
[13] T. Michler, T. Freitas, H. Oesterlin, C. Fischer, K. Wackermann, F. Ebling, Tensile testing in high pressure gaseous hydrogen using conventional and tubular specimens: Austenitic stainless steels, Int. J. Hydrogen Energy 48 (65) (2023) 25609–25618, http://dx.doi.org/10.1016/j.ijhydene.2023.03.248.
[14] K. Kumar, K. Madhusoodanan, R. Singh, Miniature test techniques for life management of operating equipment, Nucl. Eng. Des. 323 (2017) 345–358, http://dx.doi.org/10.1016/j.nucengdes.2017.03.007.
[15] Y. Madi, C. Belhadj, A. van Gorp, L. Dodelin, M. Polo, R. Goti, C. Soret, J. Besson, F. Dupoiron, Caractérisation de la température de transition et de la ténacité sur prélèvements quasi non destructifs, in: Symposium Scientifique Et Technique Esope, FCTM-ESOPE, Paris, France, 2021, URL https://hal.science/hal-03691096.
[16] O. Zvirko, I. Dzioba, M. Hredil, R. Pała, O. Oliynyk, P. Furmańczyk, Specimen size effect on the tensile properties of rolled steel of long-term-operated portal crane, Materials 16 (8) (2023) 3017, http://dx.doi.org/10.3390/ma16083017.
[17] A. Khodadad Motarjemi, M. Koçak, V. Ventzke, Mechanical and fracture characterization of a bi-material steel plate, Int. J. Press. Vessels Pip. 79 (3) (2002) 181–191, http://dx.doi.org/10.1016/S0308-0161(02)00012-1.
[18] I. Scheider, W. Brocks, A. Cornec, Procedure for the determination of true stress-strain curves from tensile tests with rectangular cross-section specimens, J. Engng Mater. Technol. 126 (1) (2004) 70–76.
[19] J.D. Lord, B. Roebuck, R. Morrell, T. Lube, 25 Year perspective aspects of strain and strength measurement in miniaturised testing for engineering metals and ceramics, Mater. Sci. Technol. 26 (2) (2010) 127–148, http://dx.doi.org/10.1179/026708309X12584564052012.
[20] M. Scibetta, E. Lucon, E. Van Walle, Optimum use of broken charpy specimens from surveillance programs for the application of the master curve approach, Int. J. Fract. 116 (2002) 231–244.
[21] N. Miura, N. Soneda, Evaluation of fracture toughness by master curve approach using miniature C(T) specimens, Trans ASME, J. Pressure Vessel Technol. 134 (2) (2012).
[22] M. Li, R. Chaouadi, I. Uytdenhouwen, T. Pardoen, G. Bonny, The Effect of Loss of Constraint on the Initiation of Ductile Fracture in a Mini-CT, in: Codes & Standards Pressure Vessels and Piping Conference, vol. 1, 2023, V001T01A035, http://dx.doi.org/10.1115/PVP2023-106216.
[23] ASTM-1820, Standard Test Method for Measurement of Fracture Toughness, Tech. rep, 2017.
[24] Z. Shokeir, J. Besson, C. Belhadj, T. Petit, Y. Madi, Edge tracing technique to study post-necking behavior and failure in al alloys and anisotropic plasticity in line pipe steels, Fatigue and Fract. Engng Mater. Struct. (2022) http://dx.doi.org/10.1111/ffe.13754.
[25] F. Albright, J. Bennin, G. Lucas, T. Wallenfelt, A Study of the Resolution of Closed Loop Servohydraulic Materials Testing Systems, Tech. rep, MTS Systems Corp., Minneapolis, MN, 1998.
[26] R. Gettu, B. Mobasher, S. Carmona, D.C. Jansen, Testing of concrete under closed-loop control, Adv. Cem. Based Mater. 3 (2) (1996) 54–71, http://dx.doi.org/10.1016/S1065-7355(96)90072-3.
[27] B. Somerday, P. Sofronis, K. Nibur, C. San Marchi, R. Kirchheim, Elucidating the variables affecting accelerated fatigue crack growth of steels in hydrogen gas with low oxygen concentrations, Acta Mater. 61 (16) (2013) 6153–6170, http://dx.doi.org/10.1016/j.actamat.2013.07.001.
[28] C. San Marchi, B.P. Somerday, K.A. Nibur, Development of methods for evaluating hydrogen compatibility and suitability, Int. J. Hydrogen Energy 39 (35) (2014) 20434–20439, http://dx.doi.org/10.1016/j.ijhydene.2014.03.234.
[29] F. Knieps, M. Köhl, M. Merklein, Influence of specimen geometry and strain rate on elongation in tensile testing of packaging steel, in: ESAFORM 2021, 2021, http://dx.doi.org/10.25518/esaform21.3876.
[30] Y. Zhao, Y. Guo, Q. Wei, T. Topping, A. Dangelewicz, Y. Zhu, T. Langdon, E. Lavernia, Influence of specimen dimensions and strain measurement methods on tensile stress–strain curves, Mater. Sci. Eng. A 525 (1–2) (2009) 68–77, http://dx.doi.org/10.1016/j.msea.2009.06.031.

[31] C.H. Suh, Y.-C. Jung, Y.S. Kim, Effects of thickness and surface roughness on mechanical properties of aluminum sheets, J. Mech. Sci. Technol. 24 (10) (2010) 2091–2098, http://dx.doi.org/10.1007/s12206-010-0707-7.
[32] Y. Takeda, C. Kiattisaksri, M. Aramaki, S. Munetoh, O. Furukimi, Effects of specimen thickness in tensile tests on elongation and deformation energy for industrially pure iron, ISIJ Int. 57 (6) (2017) 1129–1137, http://dx.doi.org/10.2355/isijinternational.ISIJINT-2016-555.
[33] Y. Shinohara, Y. Madi, J. Besson, Anisotropic ductile failure of a high-strength line pipe steel, Int. J. Fract. 197 (2016) 127–145, http://dx.doi.org/10.1007/s10704-015-0054-x.
[34] J. Besson, R. Foerch, Object-oriented programming applied to the finite element method part I. General concepts, Rev. Eur. Eléments Finis 7 (5) (1998) 535–566, http://dx.doi.org/10.1080/12506559.1998.10511321.
[35] D.L. Pinto, A.E.O. Tuhami, N. Osipov, Y. Madi, J. Besson, Simulation of hydrogen embrittlement of steel using mixed nonlocal finite elements, Eur. J. Mech. A Solids (2023) 105116, http://dx.doi.org/10.1016/j.euromechsol.2023.105116.
[36] L. Briottet, I. Moro, P. Lemoine, Quantifying the hydrogen embrittlement of pipeline steels for safety considerations, Int. J. Hydrogen Energy 37 (22) (2012) 17616–17623, http://dx.doi.org/10.1016/j.ijhydene.2012.05.143.
[37] T. Michler, K. Wackermann, F. Schweizer, Review and assessment of the effect of hydrogen gas pressure on the embrittlement of steels in gaseous hydrogen environment, Metals 11 (4) (2021) 637, http://dx.doi.org/10.3390/met11040637.
[38] N. Nanninga, Y. Levy, E. Drexler, R. Condon, A. Stevenson, A. Slifka, Comparison of hydrogen embrittlement in three pipeline steels in high pressure gaseous hydrogen environments, Corros. Sci. 59 (2012) 1–9, http://dx.doi.org/10.1016/j.corsci.2012.01.028.
[39] C. Soret, Strain-based design of pipelines in extreme environments (Ph.D. thesis), (2017PSLEM044) Université Paris sciences et lettres, 2017, URL https://pastel.hal.science/tel-01845069.
[40] D.F. Sarzosa, R.F. Souza, C. Ruggieri, J –CTOD relations in clamped SE(T) fracture specimens including 3-D stationary and growth analysis, Eng. Fract. Mech. 147 (2015) 331–354, http://dx.doi.org/10.1016/j.engfracmech.2015.05.014.
[41] W. Khor, A CTOD equation based on the rigid rotational factor with the consideration of crack tip blunting due to strain hardening for SEN(B), Fatigue Fract. Eng. Mater. Struct. 42 (7) (2019) 1622–1630, http://dx.doi.org/10.1111/ffe.13005.
[42] M. Verstraete, R. Denys, K. Van Minnebruggen, S. Hertelé, W. De Waele, Determination of CTOD resistance curves in side-grooved single-edge notched tensile specimens using full field deformation measurements, Eng. Fract. Mech. 110 (2013) 12–22.
[43] Measurement of Crack-Tip Opening Displacement (CTOD) Fracture Resistance Curves Using Single-Edge Notched Tension (SENT) Specimens, Technical Report, ExxonMobil Upstream Research Company, 2010.
[44] J.W. Hutchinson, Fundamentals of the phenomenological theory of nonlinear fracture mechanics, J. Appl. Mech. 50 (4b) (1983) 1042–1051, http://dx.doi.org/10.1115/1.3167187.
[45] T. Anderson, in: Taylor & Francis (Ed.), Fracture Mechanics: Fundamentals and Applications, 2005.
[46] K. Nibur, B. Somerday, Fracture and fatigue test methods in hydrogen gas, in: Gaseous Hydrogen Embrittlement of Materials in Energy Technologies, Elsevier, 2012, pp. 195–236, http://dx.doi.org/10.1533/9780857093899.2.195.
[47] Y. Wang, J. Gong, W. Jiang, A quantitative description on fracture toughness of steels in hydrogen gas, Int. J. Hydrogen Energy 38 (28) (2013) 12503–12508, http://dx.doi.org/10.1016/j.ijhydene.2013.07.033.
[48] S. Robinson, R. Stoltz, Toughness losses and fracture behavior of low strength carbon-manganese steels in hydrogen, ISBN: 978-0-89520-378-6, 1981, pp. 987–995.
[49] G. Gutierrez-Solana, M. Elices, High-pressure hydrogen behavior of a pipeline steel, ISBN: 978-0-87170-148-0, 1982, pp. 181–185.
[50] Y. Ogawa, H. Matsunaga, J. Yamabe, M. Yoshikawa, S. Matsuoka, Unified evaluation of hydrogen-induced crack growth in fatigue tests and fracture toughness tests of a carbon steel, Int. J. Fatigue 103 (2017) 223–233, http://dx.doi.org/10.1016/j.ijfatigue.2017.06.006.